A Brillouin light scattering study of the spin-wave magnetic field dependence in a magnetic hybrid system made of an artificial spin-ice structure and a film underlayer

F. Montoncello, M. T. Kaffash, H. Carfagno, et al.

COLLECTIONS

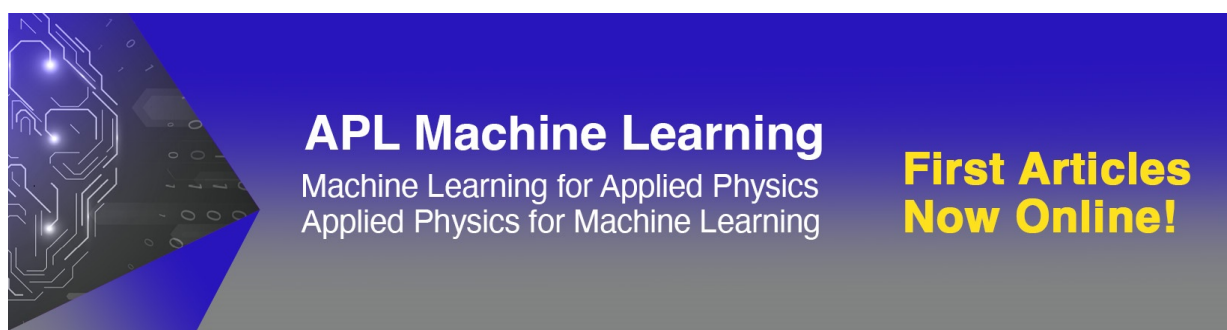Paper published as part of the special topic on Recent Advances in Magnonics

View Online   Export Citation   CrossMark

A Brillouin light scattering study of the spin-wave magnetic field dependence in a magnetic hybrid system made of an artificial spin-ice structure and a film underlayer

F. Montoncello,[1] (ID) M. T. Kaffash,[2] (ID) H. Carfagno,[3] (ID) M. F. Doty,[3] (ID) G. Gubbiotti,[4] (ID) and M. B. Jungfleisch[2,a)] (ID)

AFFILIATIONS

[1]Dipartimento di Fisica e Scienze della Terra, Università di Ferrara, Ferrara, Italy
[2]Department of Physics and Astronomy, University of Delaware, Newark, Delaware 19716, USA
[3]Department of Materials Science and Engineering, University of Delaware, Newark, Delaware 19716, USA
[4]Istituto Officina dei Materiali del Consiglio Nazionale delle Ricerche (IOM-CNR), c/o Dipartimento di Fisica e Geologia, Perugia I 06123, Italy

Note: This paper is part of the Special Topic on Recent Advances in Magnonics.
[a)]**Author to whom correspondence should be addressed:** mbj@udel.edu

ABSTRACT

We present a combined Brillouin light scattering (BLS) and micromagnetic simulation investigation of the magnetic-field-dependent spin-wave spectra in a hybrid structure made of permalloy (NiFe) artificial spin-ice (ASI) systems, composed of stadium-shaped nanoislands, deposited on the top of an unpatterned permalloy film with a nonmagnetic spacer layer. The thermal spin-wave spectra were recorded by BLS as a function of the magnetic field applied along the symmetry direction of the ASI sample. Magneto-optic Kerr effect magnetometry was used to measure the hysteresis loops in the same orientation as the BLS measurements. The frequency and the intensity of several spin-wave modes detected by BLS were measured as a function of the applied magnetic field. Micromagnetic simulations enabled us to identify the modes in terms of their frequency and spatial symmetry and to extract information about the existence and strength of the dynamic coupling, relevant only to a few modes of a given hybrid system. Using this approach, we suggest a way to understand if the dynamic coupling between ASI and film modes is present or not, with interesting implications for the development of future three-dimensional magnonic applications and devices.

Published under an exclusive license by AIP Publishing. https://doi.org/10.1063/5.0140866

I. INTRODUCTION

Artificial spin ice (ASI), arrays of nanopatterned magnetic materials, offers rich physics owing to a variety of magnetic ordering in the lattice.[1–12] These systems are particularly attractive for realizing reconfigurable magnonic crystals and devices. The reconfiguration of the magnetic ordering can be driven by an external magnetic field stimulus, which, in turn, enables the manipulation of the spin-wave propagation characteristics, i.e., the peculiar profile of the spin-wave (SW) dynamics. The dynamics profile can be more or less uniform, confined in a restricted area of the primitive periodic cell,[13] or extended over a larger area. The specific

dynamics of a spin-wave mode determine the Brillouin light scattering (BLS) intensity, the mode bandwidth, and the group velocity.[10,11,14,15] A thorough understanding of how the magnetic field affects the dynamics enables precise control of the entire system dynamics. There has been significant progress in studies of the dynamics in two-dimensional lattices. More recently, studies have transitioned to the exploration of three-dimensional systems,[16] such as magnetic multilayered systems and systems in which unpatterned films interface with patterned nanostructures (e.g., ASI).[13,17] These studies address the question of how the vertical coupling can influence the in-plane spin-wave propagation properties either through

the static interaction (generating a non-uniform internal effective field distribution, B_{eff}) or the dynamic interaction (generating hybridized states between the magnetic oscillations in distinct layers).

Here, we use both BLS and micromagnetic simulations to investigate how the biasing magnetic field affects the spin-wave dynamics in a permalloy hybrid structure comprising an ASI lattice patterned on a continuous permalloy film with nonmagnetic spacer layers of varying thickness. The ASI lattice is formed by elongated nanoelements ("islands," in the following) to mimic the bistability of atomic spins in crystalline spin ice. The results presented here go beyond our previous work,[13] where the "dispersion curves" of spin waves at a particular field value were studied. We, here, address the question of how the eigenmodes evolve as a function of the externally applied field for a fixed wavevector. In particular, we discuss the field dependence of both static and dynamic magnetization and derive the concept of dynamic coupling (i.e., mode coupling, and not static dipolar interaction) from the field evolution of the modes, illustrating how the same system can exhibit modes showing coupling while other modes do not. This is an emerging coupling mechanism that has implications for designing devices for wave-based computing.

The observed field-dependent dynamics are compared to the static magnetization configuration obtained by magneto-optic Kerr effect (MOKE) measurements. We reveal how the ASI microstate affects the film, both in its static and dynamic properties. Furthermore, we demonstrate how the SW properties depend on the static coupling (through B_{eff}) and the dynamic coupling of dipolar nature (through a hybridization of modes in the layers). The role of the coupling strength is determined by varying the separation between film and ASI layers using a nonmagnetic spacer layer. We observe rich BLS spectra in which we analyze the frequency intervals where the coupling between ASI and film is present as indicated by typical crossing/anticrossing behaviors. The experimental results are interpreted using micromagnetic simulations confirming the formation of hybridizations between ASI and film modes. While our results are derived from a specific ASI/film hybrid system, they have broad implications for more complex three-dimensional systems and suggest general strategies for the investigation of such systems.

II. EXPERIMENTAL APPROACH AND MICROMAGNETIC FRAMEWORK

A. Sample fabrication and characterization

A multi-step lithography process was used for sample fabrication. First, we define the alignment marks on a thermally oxidized Si substrate using optical lithography, electron-beam evaporation of 10 nm Ti and 50 nm Au, and lift-off. Second, we defined different underlayer/ASI structures by a combination of optical lithography, electron-beam lithography, and electron-beam evaporation. The order in which these fabrication steps are performed is varied to create the four test structures listed in Table I:

(a) continuous $Ni_{81}Fe_{19}$ film (15 nm) (Sample #1), (b) square ASI made of 15-nm thick $Ni_{81}Fe_{19}$ without underlayer film (Sample #2), (c) $Ni_{81}Fe_{19}$ (15 nm) with a 2 nm-thick naturally oxidized spacer layer and a square ASI made of 15-nm thick $Ni_{81}Fe_{19}$, and (d) $Ni_{81}Fe_{19}$ (15 nm)/Al_2O_3 (10 nm) with a square ASI made of 15-nm thick $Ni_{81}Fe_{19}$. ASI elements are composed of stadium-

TABLE I. Overview of the geometric parameters of the investigated samples: NiFe continuous (unpatterned) film (Sample #1), isolated ASI made by NiFe islands (Sample #2), hybrid film plus ASI systems with different thicknesses of the nonmagnetic spacer (Samples #3 and #4).

Sample	Film (nm)	Al_2O_3 thickness (nm)	ASI (nm)
#1	15	…	…
#2	…	…	15
#3	15	2	15
#4	15	10	15

shaped nanoislands with lateral dimensions of $260 \times 90\ nm^2$ arranged into a square lattice with lattice constant 355 nm. The film/ASI samples #3 and #4 consist of the same ASI structure as Sample #2. A representative scanning electron microscopy image is shown in Fig. 1 (here shown as Sample #2). Longitudinal hysteresis loops were measured by MOKE magnetometry at room temperature using a photoelastic modulator operating at 50 kHz and lock-in amplification. The external magnetic field, applied parallel to the vertical islands (y-direction as shown in Fig. 1), was swept in the field range between -200 and $+200$ mT. Thermally excited spin-wave spectra were measured in the backscattering configuration by BLS in the same magnetic field range and orientation. For this purpose, a monochromatic laser ($\lambda = 532$ nm) with 200 mW output power is focused onto the sample surface with a spot size of about $30\ \mu m$ in diameter. The inelastically scattered light was analyzed in frequency using a (3+3)-pass tandem Fabry–Pérot interferometer. We measure the frequency dependence of the applied magnetic field strength with the angle of incidence of the light fixed at $\theta = 10°$, which corresponds to an in-plane SW wavenumber $k = 0.41 \times 10^7$ rad/m, where $k = (4\pi/\lambda) \times \sin\theta$. This wavevector value was found to better resolve the different BLS peaks while not changing the resonance frequency compared to $k = 0$ (see also Ref. 13).
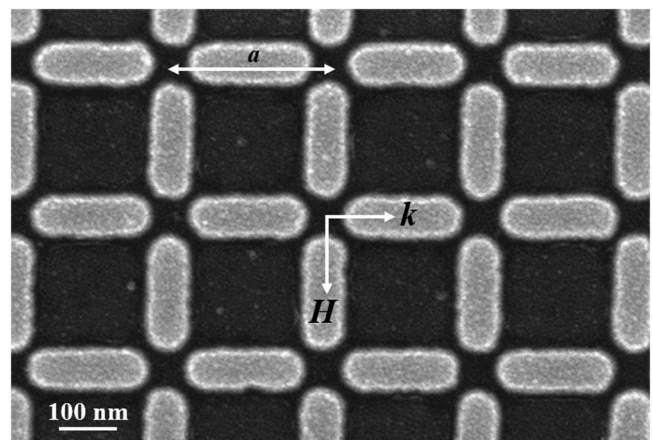

FIG. 1. Scanning electron microscopy (SEM) image of the artificial spin-ice structure. White arrows indicate the reference system together with the direction of the (positive) applied magnetic field (H) and of the in-plane component of the light transferred wavevector (k). The lattice constant a is approximately 355 nm.

B. Micromagnetic framework and simulations

Micromagnetic simulations are performed to reproduce both the static and dynamic properties of the sample by using the graphic processing unit (GPU) accelerated software mumax[3] (Ref. [18]). The micromagnetic system was designed as a 15-nm-thick layer onto a 15-nm-thick primitive cell of the ASI lattice and discretized in $4.0625 \times 4.0625 \times 5$ nm^3 micromagnetic cells. Even though the real islands are stadium-shaped, we found a better agreement using ASI elements modeled as ellipses with dimensions 64×24 cells, i.e., 260×97.5 nm^2. We attribute this to the edge oxidation of real islands, which determines an effective magnetic shape different from the geometric one (see also the supplementary material). The primitive cell is a 88×88 square (i.e., 357.5×357.5 nm^2) in which two ellipses are included. We use periodic boundary conditions to simulate a large system. The magnetic parameters are: saturation magnetization $M_s = 800$ kA/m, exchange stiffness parameter $A = 13$ pJ/m, and gyromagnetic ratio $\gamma = 185$ rad GHz/T.

The external magnetic field is applied in the range -200 to $+200$ mT and it is tilted by an angle of $1°$ to meet realistic conditions. The magnetization loops (which we compare to the MOKE measurements) are simulated from a saturated state in the y-direction in steps of 1 mT. At each field step, the relaxed state (found using a fictitious large damping factor $\alpha = 0.9$ to speed up convergence) is saved. The relaxed state is then used for the corresponding dynamical simulations (where α is set to zero): a uniform sinc pulse is applied perpendicular to the plane to determine the hybrid system's dynamics,

$$b(t) = b \frac{\sin 2\pi f_0 (t - t_0)}{2\pi f_0 (t - t_0)},$$

with $b = 1$ mT and $f_0 = 25$ GHz. The 2D profile map of the out-of-plane magnetization of the ASI-film hybrid system is recorded at a sampling time of 20 ps for a total duration of 20 ns. Then, the space-resolved time Fast Fourier Transform (FFT) is applied to the magnetization maps of the individual layers of the hybrid ASI-film system, identifying the contributions of either the ASI or the film layer. The distinct ASI and film layer spectra of the hybrid system are then superposed with a weight chosen to agree with the intensity found in experiment. The reason for that is that the (single layer) FFT calculation is not normalized, so the relative height of the peaks between different calculations (for ASI and film) is not physical and an arbitrary weight is needed for the superposition. The SW spatial profile shown throughout the manuscript corresponds to the real part of the FFT coefficients of each cell in the simulated primitive cell.[19] The BLS spectra are calculated by integrating the amplitude over all micromagnetic cells in the primitive cell ($k=0$) and then taking its square modulus (compare to theory in Ref. [20]). The field step used for the dynamic simulations was not fixed, but varied from $\Delta\mu_0 H = 25$ mT, where curves are smooth and almost linear to $\Delta\mu_0 H = 5$ mT in transition regions and at turning points.

III. RESULTS

In Fig. 2, we compare the measured MOKE hysteresis loops for all investigated samples with the simulated loops and find a
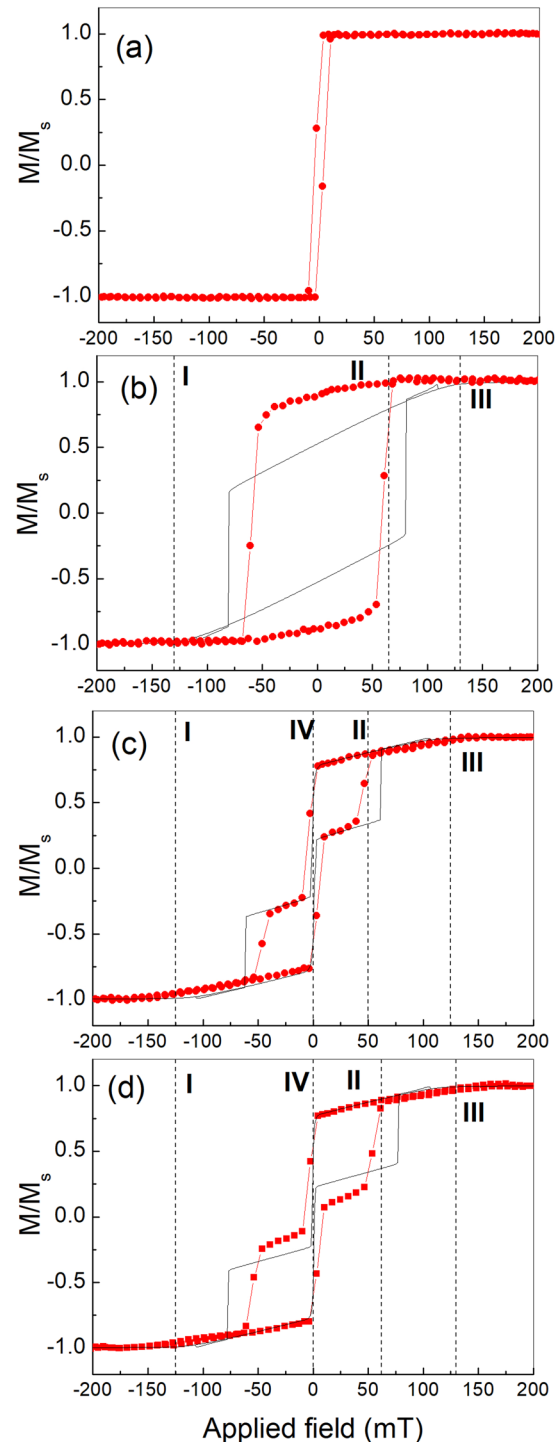

FIG. 2. Measured (red symbols) and calculated (black line) hysteresis loops for (a) uncoupled film Sample #1, (b) uncoupled ASI Sample #2, (c) coupled ASI/film Sample #3, and (d) coupled ASI/film Sample #4. The vertical lines with roman numbers mark the notable field points discussed in the text.

reasonably good qualitative agreement. For the unpatterned NiFe film [Sample #1, Fig. 2(a)], the measured MOKE loop resembles the shape of a step function, where the magnetization is almost saturated over the entire field range, except for a narrow (<1 mT) interval around $\mu_0 H = 0$, where the magnetization switches to negative values. For the isolated ASI system [Sample #2, Fig. 2(b)], the loop is characterized by an initial gradual decrease of the magnetization as the field magnitude is decreased, indicating a gradual rotation of the magnetization in the horizontal islands to the easy axis (in x-direction), followed by a sharp jump attributed to the magnetization reversal of the vertical island (identified by the vertical line II). In the other two cases [Sample #3 and Sample #4], i.e., the coupled ASI/film samples, an additional third effect is observed: the magnetization reversal of the underlying film is seen when the field is swept across 0 mT (indicated by the vertical line IV). Hence, in these two cases, there is a field region, delimited by the vertical lines IV and II, within which the magnetizations in the film and the vertical island are antiparallel. We note that such a field region occurs for both positive and negative applied magnetic fields, but for clarity, lines IV and II denote the boundaries of just one such region (for positive applied fields).

In the measurements, line II for the ASI/film systems [Figs. 2(c) and 2(d)] slightly increases from 53 to 60 mT, and the region between line IV (i.e., $B = 0$) and line II is characterized by an average relative magnetization around $M/M_s = 0.25$. In the simulation, this region is apparently wider. This mismatch between theory and experiment is due to the unavoidable distribution of

shapes across the real ASI array, which tends to smooth out discontinuities. For this reason, the actual experimental field range for region IV-II is somewhat smaller than the calculated one. The same can be said for the reversal fields of the vertical island.

As is apparent from Fig. 2, the qualitative agreement between measurements and simulations is remarkable considering the dispersion in island shape and separations between islands in the real samples. In particular, both experiment and simulation show how the region delimited by the vertical lines IV and II increases with increasing the thickness of the non-magnetic spacer: measured (simulated) line II occurs for Sample #3 at 53 mT (60 mT) and for Sample #4 at 60 mT (77 mT).

This effect can be understood by inspecting the simulation results: first of all, the film layer undergoes reversal across 0 mT through a step-like rotation (as opposed to gradual rotation) occurring within a range of around 2 mT: in this range, the magnetization of the film is mismatched with respect to that of the vertical island, which, hence, experiences strong demagnetizing fields. After the film layer switches, the magnetization texture in the vertical island is more distorted if ASI and film layers are closer to each other (as a consequence of the stronger dipolar interaction). Hence, the vertical islands undergo magnetization reversal more easily when on top of a small spacer layer than they do when the spacer layer is larger. As a result, field line II occurs at a larger value for the sample with a thicker spacer. For external magnetic fields above field line II, and, hence after the vertical island reversal, the magnetization asymptotically approaches saturation [Fig. 3(a)]. We further note that the
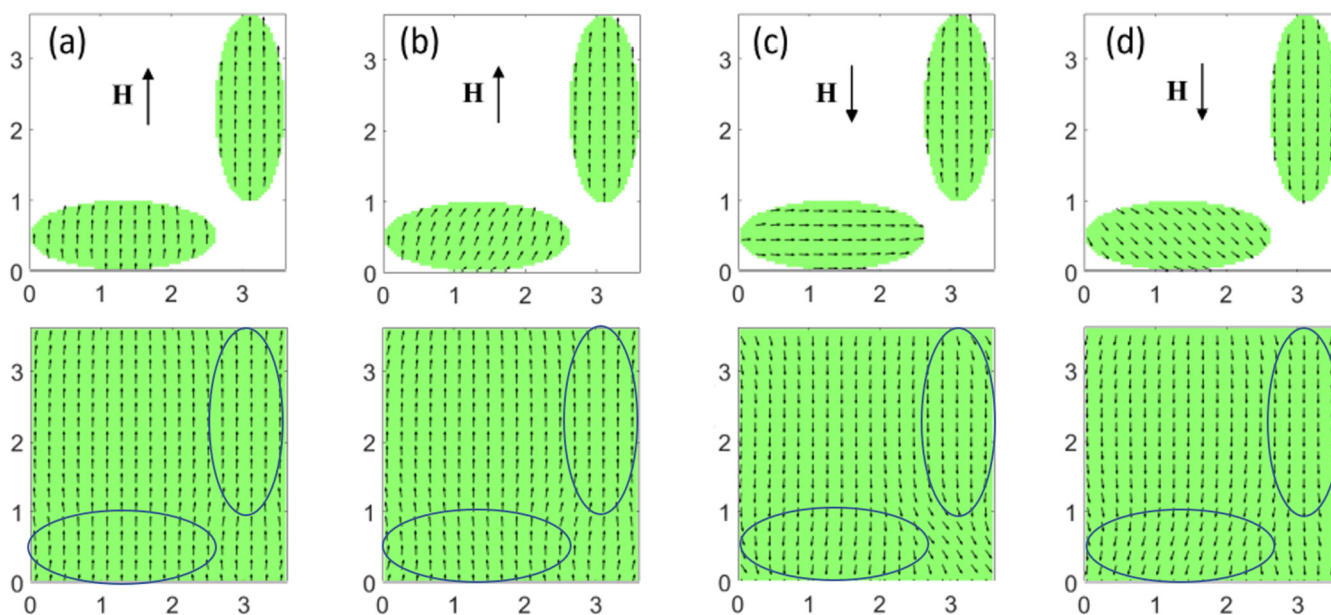

FIG. 3. Calculated static magnetization maps for ASI/film Sample #3 (top panels: ASI layer, bottom panels: film layer, outlines in the bottom panel indicate where the ASI elements are located on the maps of the underlayer). A similar scenario is found for Sample #4 (larger spacer thickness). The following field ranges are shown: (a) −200 mT to field line I ("onion states"); (b) maps at −100 mT, illustrative of any case after field line I ("S-states"); (c) +10 mT illustrative of region IV-II, after film reversal, i.e., field line IV; and (d) +60 mT, illustrative of cases after field line II. Note that arrows are only illustrative, being each one the average of a grouping of five micromagnetic cells. The units on the axes are ×100 nm.

system behaves symmetrically at positive and negative applied magnetic field values: indeed, after line II, the magnetization maps at $\pm\mu_0 H$ are indistinguishable (180° rotation).

Furthermore, we address a subtle effect that is not visible in static measurements, but only in simulations, which is marked by the field lines I and III (Fig. 2): at these field values (± 125 mT), a barely appreciable change of slope in the simulated magnetization curves occur, due to the reorientation of the magnetization in the horizontal islands (change of symmetry) from an onion state to a S-state at line I (and vice versa, at line III). The different symmetries of the magnetization maps can be seen in the illustrative panels (a) and (b) in Fig. 3. Experimental observation of onion and S-states were discussed in Refs. 21–23. Nevertheless, this barely appreciable change produces a remarkably visible effect in the dynamics, i.e., a definite minimum in the SW frequency-field curve corresponding to peak (2),[5,24,25] which is discussed below in more detail.

Moreover, we observe how the measured MOKE loops for the NiFe film/ASI samples #3 and #4 [(Figs. 2(c) and 2(d)] show very sharp transitions with switching fields that do not differ significantly from those of the isolated film and ASI samples [(Figs. 2(a) and 2(b)]. This suggests that the film and ASI layers are weakly coupled only by magnetostatic interaction (as opposed to exchange interaction).

In the following, we describe the frequency-field behavior investigated by BLS, which we show as false-color coded plots in Fig. 4, and discuss it in relation to the simulation results. We recall that, in our BLS measurements, the incidence plane was aligned perpendicularly to the applied field direction [Damon–Eshbach (DE) configuration]. To investigate the frequency vs field dependence, we first saturate the sample magnetization with a large magnetic field of -200 mT along the y-direction [see the simulated map in Fig. 3(a)] and then sweep the field to positive saturation ($+200$ mT) in steps of 5 mT following the ascending branch of the hysteresis loop.[26] The false-color intensity scale in Fig. 4 presents the anti-Stokes side of the measured BLS spectra (positive frequency shift of light). Note that the measured MOKE loops (red dots) are superimposed in the same panels (a)–(d) to link the changes in the magnetization configuration to the field-dependent frequency behavior of the SW modes. In addition, we show the raw BLS spectra, together with the simulated ones, at $\mu_0 H = -200$ mT in panels (e)–(h). For the unpatterned film (Sample #1), only one peak is observed in the spectrum corresponding to the DE mode. Its frequency-field curve exhibits the typical V-shape behavior centered about a zero field, i.e., an almost linear dependence with symmetric values for negative and positive fields. This behavior coincides with the abrupt magnetization switching observed in the MOKE loop at a zero field. The DE analytical curve is plotted as a reference, calculated for consistency with the measured one but differently from the next simulations, at $k = 0.41 \times 10^7$ rad/m.[27,28]

For the ASI Sample #2 shown in Fig. 4(b), two larger intensity peaks [labeled as (1) and (2)] and a less intense one labeled as (3) are observed. Comparing these peaks to the simulations, we can associate them to the fundamental mode of the vertical island F_v [peak (1)], the edge mode of the horizontal island EM_h [peak (2)], and the fundamental mode of the horizontal island F_h [peak (3)]. The calculated phase amplitude profiles of these modes are shown

in Fig. 5. F_v [peak (1)] belongs to the vertical island, which, due to the shape anisotropy, does not exhibit significant variation of its magnetization as the applied field magnitude is decreased to zero. This indicates an almost constant effective gyromagnetic ratio,[5,29] i.e., a constant slope down to a zero field (Larmor-like behavior). The frequency-field curve involving peak (2), i.e., mode EM_h, is characterized by the typical "W-shape" behavior due to the competition between the applied field and the shape anisotropy of the involved island (in this case, the horizontal one). The frequency minima at ± 125 mT are due to the sudden change of the slope of the magnetization curve as evidenced in Fig. 4 by field line I and III. In Ref. 24, this kind of magnetization change was studied as a second order transition, which can typically be found in any elongated nano-element (either isolated or in a lattice) initially magnetized along the short axis.[4,5,11,15,30,31]

Interestingly, at around -80 mT, peaks (2) and (3), i.e., EM_h and F_h (Fig. 4), undergo an obvious anticrossing ("mode repulsion," as evidenced by the formation of a "gap" in the spectrum), after which the corresponding modes exchange their character, and invert the slope of their curves (see comments in Ref. 32). The repulsion seems to be absent when the film and ASI layer couple, see Samples #3 and #4 [Fig. 4(c) and 4(d)]. Close to a zero field, peak (3) [which after -80 mT has gained the "fundamental-mode" character of previous peak (1)] intersects peak (2) at about 9.2 GHz: this degeneracy at a zero field is a clear experimental indication that the corresponding modes (F_v and F_h) are oscillating in different regions of the sample.

In general, the magnetization distributions of these regions are different before the crossing point. At a zero field, they are indistinguishable, and, hence, they have the same resonance frequency. For the particular geometry of our ASI system, namely, a periodic cell with two islands, these regions are the two differently oriented islands in the primitive cell. At a zero field, the two islands become indistinguishable and their magnetization is exactly aligned along their long axis. As a consequence, the resonances of both islands occur at the same frequency at a zero field as evidenced by the observed mode intersection in the BLS curves. After $\mu_0 H = 0$ mT, the curves continue their specific behavior until a frequency jump (at field line II) is observed in correspondence to the magnetization reversal of the ASI vertical islands. After this switching point, the observed behavior is symmetrical with respect to the negative field part.

The SW dynamics in the hybrid ASI/film systems at $\mu_0 H = 200$ mT is reported in detail in Ref. 13, where it was found that the ASI modes with resonance frequencies below the DE mode of the uncoupled film are almost insensitive to the presence of the film underlayer: as found in the simulations, in this frequency range, the modes show in the ASI layer a phase profile almost identical to that shown in Fig. 5 for the uncoupled ASI lattice, while in the film layer, the dynamic magnetization is almost negligible.

On the other hand, in the same reference, it was found that modes close to the DE frequency can show a phase profile hybridization between ASI and film layer. This type of hybridization is called dynamic coupling. This effect, if present, is a robust link between a specific mode of the film layer and a specific mode of the ASI layer. The phase profiles of a few of these ASI/film modes (i.e., those with a frequency close to the DE mode of the film),
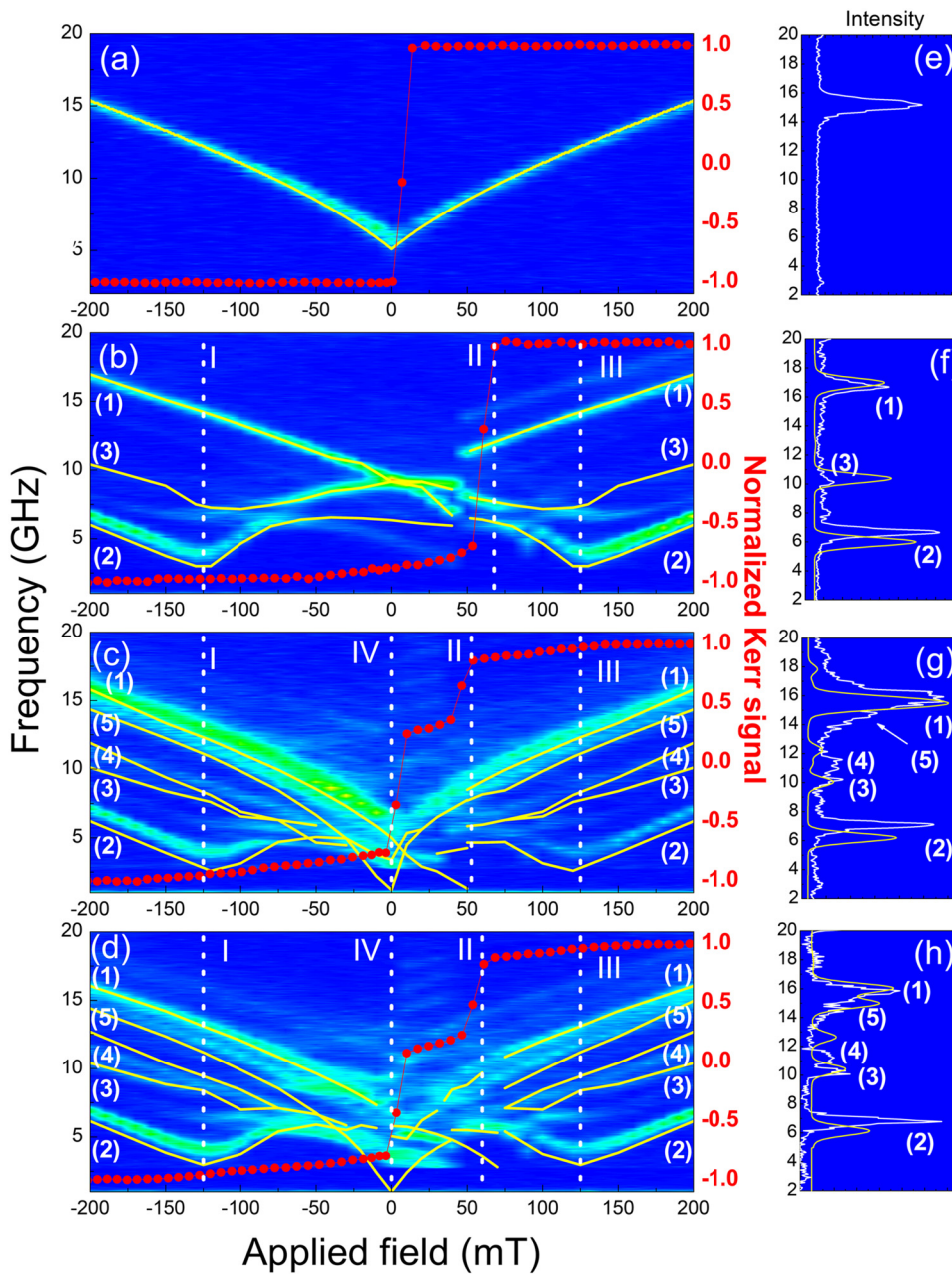
FIG. 4. Field dependence (increasing field from left to right) of the BLS spectra from thermally excited SWs measured at $k = 0.41 \times 10^7$ rad/m (color scale) for (a) Sample #1, (b) Sample #2, (c) Sample #3, and (d) Sample #4. In panel (a), the theoretical Kalinikos–Slavin curve calculated at $k = 0.41 \times 10^7$ rad/m is plotted with the measurements. In panel (b)–(d), simulations are carried out for $k = 0$ (solid lines) and are plotted together with numbers identifying the peaks in the spectra. The normalized MOKE loops (red symbols, axis on the right) are also shown for all the investigated samples. Vertical dashed lines mark the notable (transition) points discussed in the text. Panels (e)–(h) show the corresponding Stokes side of the BLS spectra (intensity vs frequency shift, same units of the vertical axis on the left) for an applied field of -200 mT, to which simulated spectra are superimposed (yellow curves).

having a relevance in the BLS spectra, are shown in Fig. 6. Mode (a), occurring at 11.9 GHz for Sample #3 (for $\mu_0 H = \pm 200$ mT), is reminiscent of the DE mode in the film. However, it now resides in the absolute minimum of the effective magnetic field well $B_{\rm eff}$ [within 1–3×100 nm along y, see panel (e)] created in the film by the static dipolar interaction between the layers: this mode does not show any dynamic coupling between ASI and film layer, since the specific phase profile in the ASI layer changes when the external field or the spacer layer thickness is changed. Mode (b) is as well

reminiscent of the DE mode of the film, but trapped in the other (relative) minimum of $B_{\rm eff}$ (within 1.5–3×100 nm along y). This minimum is shallower than the previous one, and, correspondingly, the frequency of this mode is higher than the previous mode (a), i.e., 14.4 GHz for Sample #3 at ± 200 mT. As is apparent from the two-layer phase profiles, there is a vertical correspondence between the phase amplitudes (hybridization). This correspondence is robust with respect to field or spacer thickness variations (Fig. 7): hence, this mode shows a dynamic coupling of dipolar origin
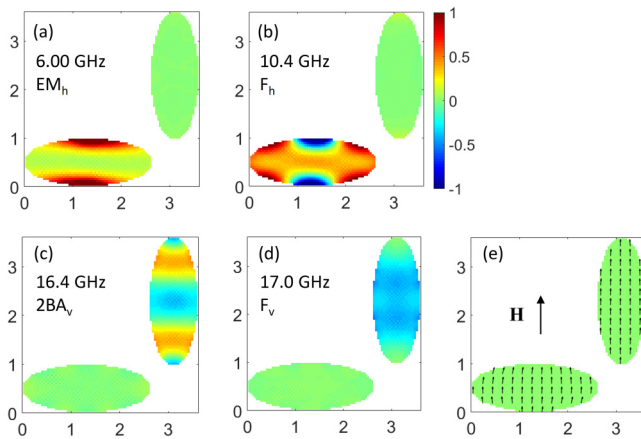
FIG. 5. SW phase amplitude profiles (arb. units) for the uncoupled ASI lattice, with the corresponding frequencies, calculated for $\mu_0 H = -200$ mT: (a) EM_h; (b) F_h; (c) $2BA_v$; (d) F_v; and (e) equilibrium magnetization distribution (each arrow corresponds to the average over five micromagnetic cells). The units on the axes are ×100 nm. Reproduced with permission from Negrello et al., APL Mater. **10**, 091115 (2022). Copyright 2022 AIP Publishing LLC.

system: without (panels on the left), and with (panels on the right) the dynamic coupling, or, in other terms, the possible persistence of the association between a specific ASI mode and a specific film mode in spite of biasing magnetic field or spacer layer thickness variations. As is apparent from Fig. 7 (panels on the left), for the mode on the left (at 200, 150, and 100 mT and, correspondingly, 11.9, 9.4, and 6.9 GHz) [i.e., the same mode as shown in Fig. 6(a) giving rise to peak (4) in the experiments], the dynamic magnetization in the associated ASI layer changes when either the applied field or the spacer thickness changes. This means that there is no link between the excitations of ASI and film layers.

On the other hand, for the mode on the right (at 200, 150, and 100 mT and, correspondingly, at 14.8, 12.9, and 10.8 GHz) [i.e., the same mode as shown in Fig. 6(c), contributing to peak (1) in the experiments], the association of the specific ASI mode with the specific film mode (in vertical correspondence) is persistent against any field or spacer variations. This is true within a range that preserves the general symmetry of the magnetization distribution. The range of values, of any of these parameters, preserving the coupling is itself an indirect quantification of such dynamic interaction. As far as this mode is concerned, we found that the coupling persists down to −75 mT, below which the profiles are hardly recognizable and the hybridization is no longer present.

As discussed in Ref. 13, the simulations suggest that modes (b)–(d) in Fig. 6 with frequencies close to one another contribute to peak (1). However, we note that occasionally mode (b) can emerge in the spectra as an independent shoulder peak (5). In particular, modes (b) and (d) can be thought of as the (theoretical) extremes of the experimental broad curve of peak (1), while mode (c) has a frequency which is intermediate. This interpretation is supported by the experiment: the BLS spectra correspondingly show a broad peak
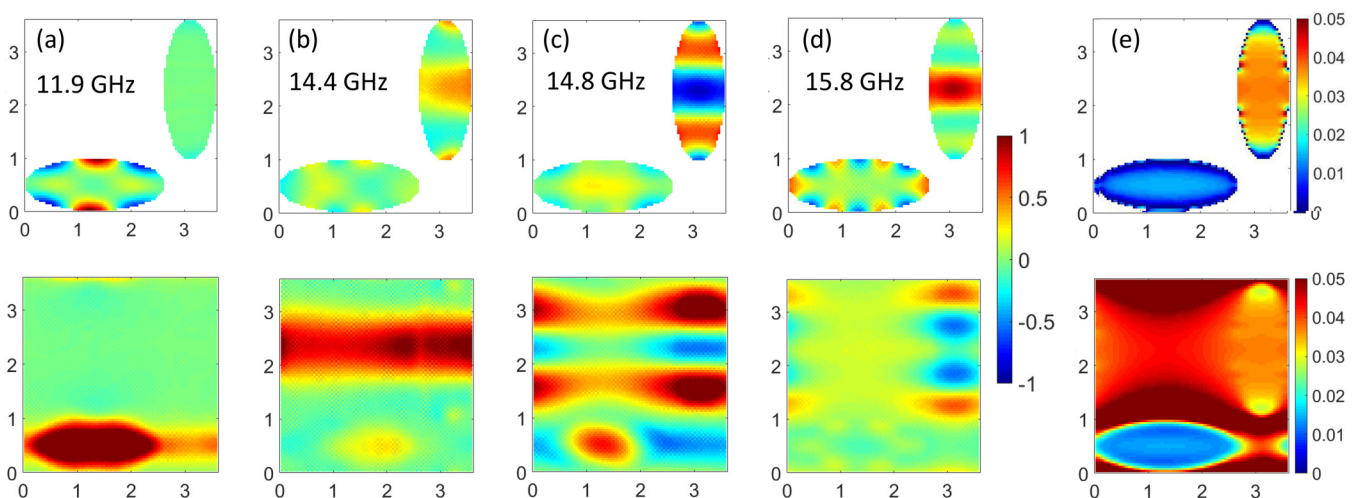
between ASI and film layers. Also, in modes (c) and (d), the dynamic coupling is apparently present: in (c), the coupling results in a phase coherence between the layers, such that ASI can imprint its dynamic nodal structure in-phase in the film, while in (d), an out-of-phase relationship is imprinted. In Fig. 7, we illustrate the different behavior of two among the many modes present in our

FIG. 6. Phase profiles (in arbitrary units) of the coupled ASI-film system (Sample #3, but indicative of Sample #4 also) for $\mu_0 H = -200$ mT applied along y: (a) mode giving the BLS peak number (4); (b) mode giving the BLS peak number (5), characterized by an ASI/film in-phase precession; (c) mode contributing to the BLS peak (1), characterized by $\lambda = a/2$ along y; (d) mode contributing to the BLS peak (1), characterized by an ASI/film out-of-phase precession; and (e) profile of the magnitude of B_{eff}, sidebar units are T. The units on the axes are ×100 nm.

at a single field value [−200 mT in Figs. 4(g) and 4(h)], and the measured curve is a broad colored band in Figs. 4(c) and 4(d) at any field value in correspondence to those modes.

In the following, we examine the detailed frequency/field curves of the hybrid ASI/film systems [i.e., Samples #3 and #4, Figs. 4(c) and 4(d)]. We observe the lowest frequency curve [due to peak (2), i.e., mode EM_h] to behave almost the same in both coupled samples, showing the typical "W-shape" behavior found in the uncoupled ASI, in particular, with the frequency minima at lines I–III. This observation can be easily understood by considering the following two facts: (1) Below, the DE mode frequency of the ASI layer is uncoupled from the film layer: the values of B_{eff} [Fig. 6(e)] experienced by the low frequency modes (in the horizontal island area) are very low (dark blue) with respect to the corresponding area in the film layer (light blue). This favors decoupled magnetization dynamics, and in our specific case, only the ASI layer is excited at these frequencies. (2) The ASI response can be understood as a superposition of its building block's responses.[31] It has been shown previously that it is possible to derive the magnetization orientation of each ASI element and the localization of the specific mode by extracting the effective gyromagnetic ratio from experimental data.[5,29]

Based on these criteria, we observe that the curves associated with peaks (1) and (3–5) decrease almost monotonically, both in experiments and simulations. This frequency decrease continues until field line IV (i.e., 0 mT) when the film undergoes magnetization reversal.

As mentioned above, mode (a) of Fig. 6, corresponding to peak (4), decreases in frequency as the field is increased from −200 mT. This mode gradually diminishes in intensity as the field crosses the value −30 mT, until the mode disappears in the spectra above −10 mT. This is also found in the simulations: we attribute this effect to the behavior of the two B_{eff} regions (wells). The simulations (Fig. 8) reveal the deepest well as the one below the horizontal island (within $0–1 \times 100$ nm along y) from −200 mT to around −30 mT. However, from about −10 mT to higher applied field values the deepest well is the upper one ($1.5–3.5 \times 100$ nm), while the former becomes shallower due to the progressive rotation of the magnetization into the long (easy) axis (x-direction). Although a thorough investigation of this phenomenon is outside the scope of the paper, we suggest that the reason lies in the depth of the B_{eff} well in the film in vertical correspondence to the horizontal island: at higher fields, this well is not sufficiently deep to host a localized
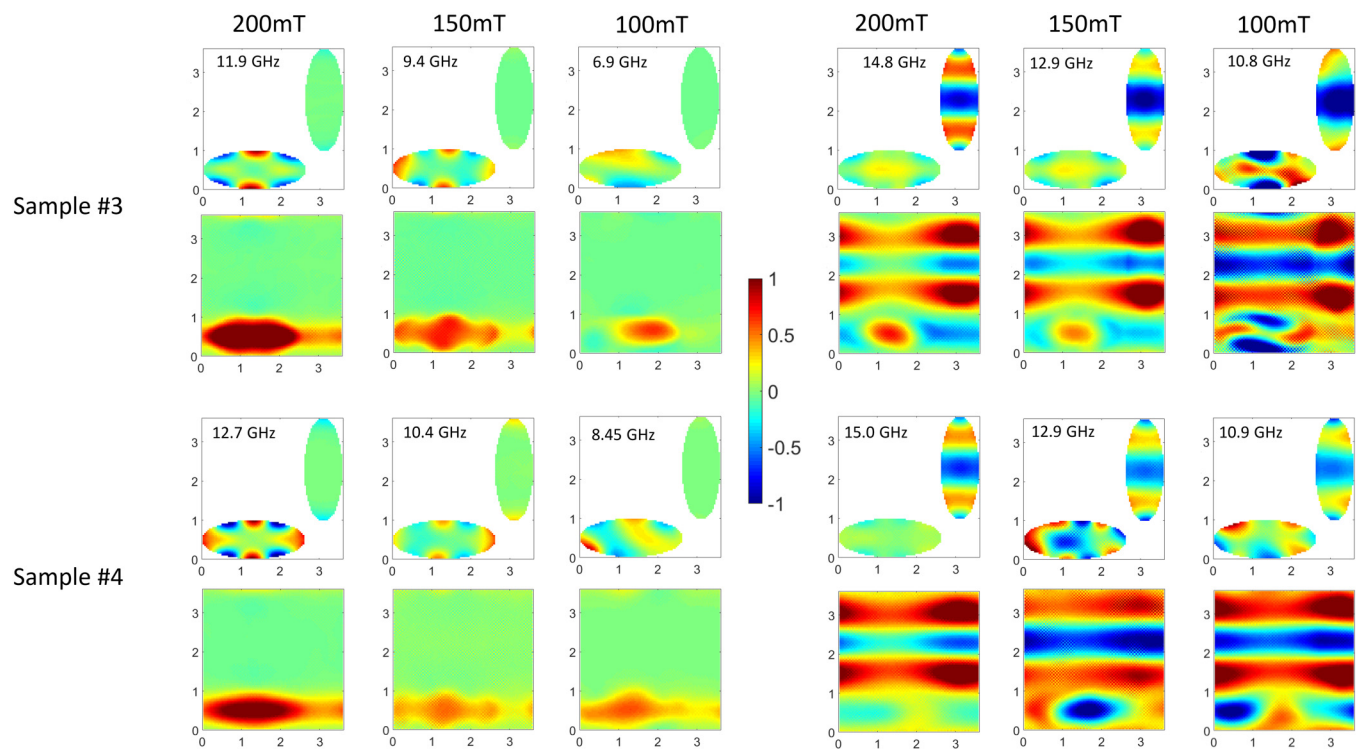

FIG. 7. Example of modes without (left) or with (right) dynamic coupling between layers, at different field values and spacer thickness (Sample #3 in upper panels, and #4 in bottom panels). For each mode, two panels are shown, corresponding to the phase amplitude profiles (in arbitrary units) in the ASI layer (top panel) and in the film layer (bottom one). In particular, on the left we plot the mode corresponding to peak (4), in which the dynamic magnetization in the ASI layer changes as field or spacer is changed (no coupling); on the right, we plot the mode giving a large BLS peak [intermediate between peak (1) and (5)], which shows a hybridization between the mode in the ASI layer (in this case, $2BA_v$) and the one in the film layer, with a phase relationship in vertical correspondence. The association persists in changing the field value of the spacer thickness (dynamic coupling). The units on the axes are $\times 100$ nm.
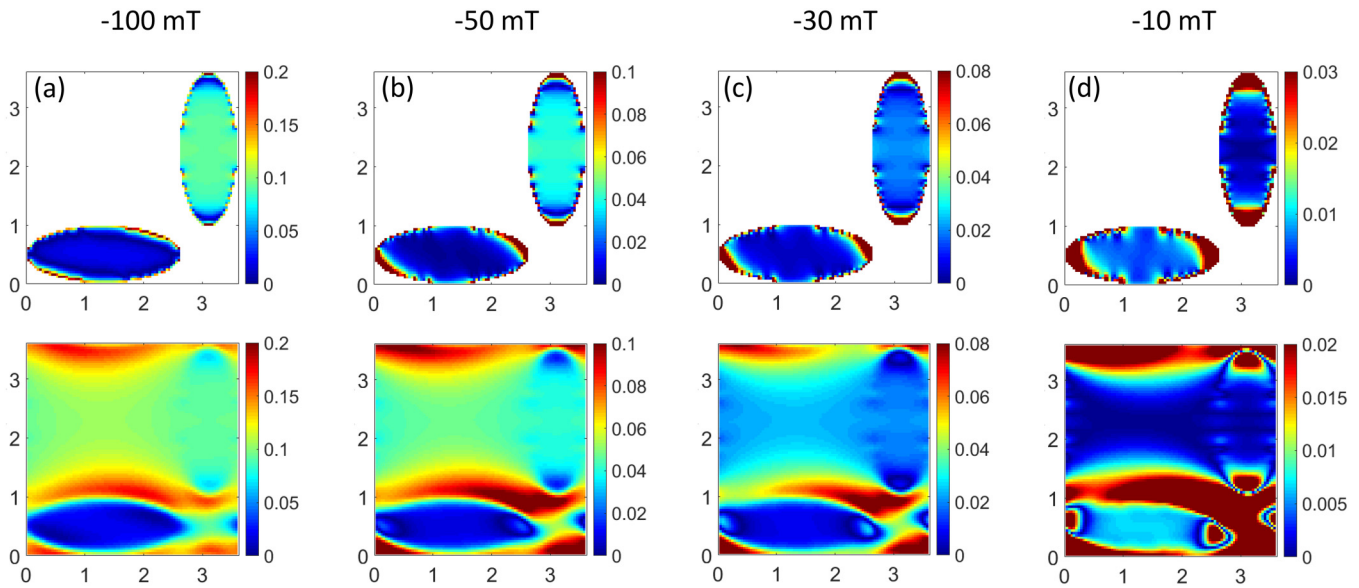
FIG. 8. Variation with the applied field of the space profile of B_{eff} in the film layer, (a) -100 mT, (b) -50 mT, (c) -30 mT, and (d) -10 mT: the colormap refers to the y component (in units of T), i.e., along H. Two regions form, separated by high value B_{eff} barriers (red), one within 0–1 (units are $\times100$ nm) is the (deepest) absolute minimum, the other within 1.5–3.5 is a (shallower) relative minimum; however, below -30 mT their role is exchanged. The units on the axes are $\times100$ nm.

excitation because the magnetic moments are better aligned and the relative demagnetizing field smaller.

Interestingly, the intensity of mode (b) in Fig. 6 [peak (5)], is rather weak at -200 mT [the mode appears in the spectra as a left shoulder to the main peak (1)], but, based on simulation results, this mode acquires intensity as soon as the field is increased, and above -180 mT, it becomes the most intense one. However, this effect could hardly be detected in the BLS experiment, which always detects a broad band.

A representative magnetization map for the range delimited by line IV and II ("IV-II region") is shown in Fig. 3(c) (here $+10$ mT). In this region IV-II, the magnetization in the film layer is (on average) parallel to the applied field (in y-direction) and as the field is further increased, it progressively becomes more aligned to the (negative) y-axis: the consequence is a frequency increase of the modes localized in the film layer [i.e., modes (a)–(d) in Fig. 6, and in particular, the mode that gives rise to peak (5)].

With reference to the simulations, we can identify four curves in this region IV-II for Samples #3 and #4: (1) the curve ascending from a minimum frequency at a zero field, corresponding to the "acoustic"-like mode (b) in Fig. 6 is identified as peak (5) in the spectra. In the ideal case, this mode should not have any (or only a small) discontinuity in crossing the field line II, where the reversal of the vertical island occurs (see Ref. 33); (2) the curve associated with peak (1) continues to decrease even after line IV (i.e., above a zero field) down to the transition point line II. This is due to the "optical" character of mode (d) in Fig. 6. This curve experiences a strong discontinuity at the transition point near line II; (3) and (4) the two curves associated with EM_h [peak (2)] and F_h [peak (3)] in

the ASI layer show negligible dynamics in the film layer. These modes are strictly localized in the horizontal islands, and their frequency depends on the magnetization map of those islands. Their frequency-field curves have an irregular behavior in the IV-II region. This is due to the fact that the magnetization of the horizontal island is perpendicular to the one of the film [Fig. 3(c)]: after line IV, the magnetization first tends to align to the easy axis coming from a configuration similar to (b) of the same figure. This alignment results in a frequency increase. After that, the magnetization realigns as is shown in panel (d) of the same figure. This realignment causes a frequency decrease. Those two modes have only a small intensity due to the specific profile and are, therefore, difficult to resolve in the experiment.

IV. CONCLUSIONS

In conclusion, we studied a "vertical magnonic structure" based on a hybrid ASI/film systems with varying spacer layer thickness by BLS spectroscopy. We correlate the measured dynamics with the magnetization loops measured by Kerr magnetometry and identify the main discontinuities in the loops as changes of the magnetization either in the film or the ASI layer. Using micromagnetic simulations, we associate each experimental BLS curve with one or more SW modes of significant intensity. Furthermore, the simulations enabled us to understand the specific dependence on the field (slope and effective gyromagnetic ratio) with considerations about the mode profile in either layer and the underlying magnetization orientations. We reveal that the internal effective field behavior determines the mode phase profiles (with their peculiar localizations) and the dynamic

relationship between the two layers and the frequency-field evolution. Our work identifies the role of dynamic coupling as an additional interaction between modes of different layers, emerging in the dynamics from the geometric complexity of the structure, which preserves the associated modes in either layer in spite of any variation of applied field or spacer thickness. This coupling must be considered a hybridization between modes of different layers, persisting within a certain range of values, which is an indirect quantification of this interaction. Investigating the field-dependent dynamics resulting from the interplay between the layers and the emerging interlayer hybridization can unveil a new degree of freedom, which is particularly useful in manipulating the spin-wave intensity profile and propagation properties. The findings have direct implications for magnonic applications including spin-wave interferometry, spin-wave logic gates and devices, spin-wave computing, and tunable dynamic magnetic metamaterials.

SUPPLEMENTARY MATERIAL

See the supplementary material for a discussion of the micromagnetic representation of the fabricated islands.

AUTHOR DECLARATIONS

Conflict of Interest

The authors have no conflicts to disclose.

DATA AVAILABILITY

The data that support the findings of this study are available from the corresponding author upon reasonable request.

REFERENCES

[1] X. Zhou, G. L. Chua, N. Singh, and A. O. Adeyeye, "Large area artificial spin ice and anti-spin ice $Ni_{80}Fe_{20}$ structures: Static and dynamic behavior," Adv. Funct. Mater. **26**, 1437–1444 (2016).

[2] E. Iacocca, S. Gliga, R. L. Stamps, and O. Heinonen, "Reconfigurable wave band structure of an artificial square ice," Phys. Rev. B **93**, 134420 (2016).

[3] S. Gliga, A. Kákay, R. Hertel, and O. G. Heinonen, "Spectral analysis of topological defects in an artificial spin-ice lattice," Phys. Rev. Lett. **110**, 117205 (2013).

[4] M. B. Jungfleisch, W. Zhang, E. Iacocca, J. Sklenar, J. Ding, W. Jiang, S. Zhang, J. E. Pearson, V. Novosad, J. B. Ketterson, O. Heinonen, and A. Hoffmann, "Dynamic response of an artificial square spin ice," Phys. Rev. B **93**, 100401 (2016).

[5] W. Bang, F. Montoncello, M. B. Jungfleisch, A. Hoffmann, L. Giovannini, and J. B. Ketterson, "Angular-dependent spin dynamics of a triad of permalloy macrospins," Phys. Rev. B **99**, 014415 (2019).

[6] V. S. Bhat and D. Grundler, "Angle-dependent magnetization dynamics with mirror-symmetric excitations in artificial quasicrystalline nanomagnet lattices," Phys. Rev. B **98**, 174408 (2018).

[7] V. S. Bhat, F. Heimbach, I. Stasinopoulos, and D. Grundler, "Magnetization dynamics of topological defects and the spin solid in a kagome artificial spin ice," Phys. Rev. B **93**, 140401 (2016).

[8] D. M. Arroo, J. C. Gartside, and W. R. Branford, "Sculpting the spin-wave response of artificial spin ice via microstate selection," Phys. Rev. B **100**, 214425 (2019).

[9] T. Dion, D. M. Arroo, K. Yamanoi, T. Kimura, J. C. Gartside, L. F. Cohen, H. Kurebayashi, and W. R. Branford, "Tunable magnetization dynamics in artificial spin ice via shape anisotropy modification," Phys. Rev. B **100**, 054433 (2019).

[10] S. Mamica, X. Zhou, A. Adeyeye, M. Krawczyk, and G. Gubbiotti, "Spin-wave dynamics in artificial anti-spin-ice systems: Experimental and theoretical investigations," Phys. Rev. B **98**, 054405 (2018).

[11] Y. Li, G. Gubbiotti, F. Casoli, F. J. T. Gonçalves, S. A. Morley, M. C. Rosamond, E. H. Linfield, C. H. Marrows, S. McVitie, and R. L. Stamps, "Brillouin light scattering study of magnetic-element normal modes in a square artificial spin ice geometry," J. Phys. D: Appl. Phys. **50**, 015003 (2016).

[12] S. Lendinez, M. T. Kaffash, and M. B. Jungfleisch, "Emergent spin dynamics enabled by lattice interactions in a bicomponent artificial spin ice," Nano Lett. **21**, 1921–1927 (2021).

[13] R. Negrello, F. Montoncello, M. T. Kaffash, M. B. Jungfleisch, and G. Gubbiotti, "Dynamic coupling and spin-wave dispersions in a magnetic hybrid system made of an artificial spin-ice structure and an extended NiFe underlayer," APL Mater. **10**, 091115 (2022).

[14] V. S. Bhat, S. Watanabe, K. Baumgaertl, A. Kleibert, M. A. W. Schoen, C. A. F. Vaz, and D. Grundler, "Magnon modes of microstates and microwave-induced avalanche in kagome artificial spin ice with topological defects," Phys. Rev. Lett. **125**, 117208 (2020).

[15] Y. Li, G. Gubbiotti, F. Casoli, S. A. Morley, F. J. T. Gonçalves, M. C. Rosamond, E. H. Linfield, C. H. Marrows, S. McVitie, and R. L. Stamps, "Thickness dependence of spin wave excitations in an artificial square spin ice-like geometry," J. Appl. Phys. **121**, 103903 (2017).

[16] G. Gubbiotti, *Three-Dimensional Magnonics: Layered, Micro- and Nanostructures* (Jenny Stanford Publishing, Singapore, 2019).

[17] E. Iacocca, S. Gliga, and O. G. Heinonen, "Tailoring spin-wave channels in a reconfigurable artificial spin ice," Phys. Rev. Appl. **13**, 044047 (2020).

[18] A. Vansteenkiste, J. Leliaert, M. Dvornik, M. Helsen, F. Garcia-Sanchez, and B. Van Waeyenberge, "The design and verification of MuMax3," AIP Adv. **4**, 107133 (2014).

[19] B. V. de Wiele and F. Montoncello, "A continuous excitation approach to determine time-dependent dispersion diagrams in 2D magnonic crystals," J. Phys. D: Appl. Phys. **47**, 315002 (2014).

[20] G. Gubbiotti, G. Carlotti, T. Okuno, M. Grimsditch, L. Giovannini, F. Montoncello, and F. Nizzoli, "Spin dynamics in thin nanometric elliptical permalloy dots: A Brillouin light scattering investigation as a function of dot eccentricity," Phys. Rev. B **72**, 184419 (2005).

[21] W. Rave and A. Hubert, "Magnetic ground state of a thin-film element," IEEE Trans. Magn. **36**, 3886 (2000).

[22]J. García, A. Thiaville, J. Miltat, K. Kirk, and J. Chapman, "MFM imaging of patterned permalloy elements under an external applied field," J. Magn. Magn. Mater. **242–245**, 1267–1269 (2002).

[23]S. Hankemeier, R. Frömter, N. Mikuszeit, D. Stickler, H. Stillrich, S. Pütter, E. Vedmedenko, and H. P. Oepen, "Magnetic ground state of single and coupled permalloy rectangles," Phys. Rev. Lett. **103**, 147204 (2009).

[24]F. Montoncello, L. Giovannini, F. Nizzoli, P. Vavassori, and M. Grimsditch, "Dynamic origin of first and second order phase transitions in magnetization reversal of elliptical nanodots," Phys. Rev. B **77**, 214402 (2008).

[25]J. K. Ha, R. Hertel, and J. Kirschner, "Micromagnetic study of magnetic configurations in submicron permalloy disks," Phys. Rev. B **67**, 224432 (2003).

[26]S. Tacchi, M. Madami, G. Gubbiotti, G. Carlotti, A. O. Adeyeye, S. Neusser, B. Botters, and D. Grundler, "Magnetic normal modes in squared antidot array with circular holes: A combined Brillouin light scattering and broadband ferromagnetic resonance study," IEEE Trans. Magn. **46**, 172–178 (2010).

[27]R. Damon and J. Eshbach, "Magnetostatic modes of a ferromagnet slab," J. Phys. Chem. Solids **19**, 308–320 (1961).

[28]B. A. Kalinikos and A. N. Slavin, "Theory of dipole-exchange spin wave spectrum for ferromagnetic films with mixed exchange boundary conditions," J. Phys. C: Solid State Phys. **19**, 7013–7033 (1986).

[29]W. Bang, J. Sturm, R. Silvani, M. T. Kaffash, A. Hoffmann, J. B. Ketterson, F. Montoncello, and M. B. Jungfleisch, "Influence of the vertex region on spin dynamics in artificial kagome spin ice," Phys. Rev. Appl. **14**, 014079 (2020).

[30]F. Montoncello, L. Giovannini, F. Nizzoli, P. Vavassori, M. Grimsditch, T. Ono, G. Gubbiotti, S. Tacchi, and G. Carlotti, "Soft spin waves and magnetization reversal in elliptical permalloy nanodots: Experiments and dynamical matrix results," Phys. Rev. B **76**, 024426 (2007).

[31]W. Bang, F. Montoncello, M. T. Kaffash, A. Hoffmann, J. B. Ketterson, and M. B. Jungfleisch, "Ferromagnetic resonance spectra of permalloy nano-ellipses as building blocks for complex magnonic lattices," J. Appl. Phys. **126**, 203902 (2019).

[32]Before -80 mT the role of the "fundamental mode" (i.e., no nodes, high intensity) is held by EM_h, while the actual F_h mode has nodes (a phase change at the edges) and a lower average amplitude. After -80 mT, because the magnetization of the horizontal elements is oriented at about $45°$, the EM_h limits its amplitude at the edges only, while F_h acquires a larger amplitude in the center.

[33]D. Kuźma, F. Montoncello, P. Sobieszczyk, A. Wal, L. Giovannini, and P. Zieliński, "Spin wave propagation properties across configurational antiferro/ferro-magnetic transitions," J. Appl. Phys. **124**, 223902 (2018).